Microwave Regenerable Nickel, Zinc Co-doped Nitrogen-Coordinated Porous Carbon Catalyst for Nitrogen Fixation

Peiji Deng,[∇] Yixian Liu,[∇] Yunliang Liu, Yaxi Li, Ruqiang Wu, Lijun Meng, Kang Liang, Yixiang Gan, Fen Qiao, Naiyun Liu,* Zhenhui Kang,* and Haitao Li*
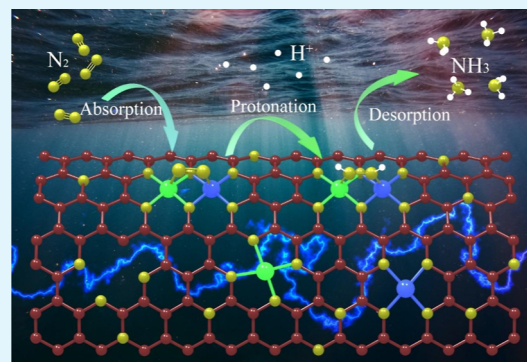
Read Online

ACCESS | Metrics & More | Article Recommendations | SI Supporting Information

ABSTRACT: More than 90% of the global NH_3 synthesis is dominated by the Haber−Bosch process, which consumes 2% of the worldwide energy and generates 1.44% of the global carbon emission. The electrochemical N_2 reduction reaction (NRR) is regarded as an attractive alternative route to produce NH_3 under mild reaction conditions, but the electrocatalysts suffer from the difficulty of N≡N cleavage. In this work, we report a leaf-like MOF-derived Ni/Zn bimetallic co-doped nitrogen-coordinated porous carbon (Ni/Zn-NPC) as a cost-effective NH_3 synthesis electrocatalyst. The resultant electrocatalyst achieved a high NH_3 production rate of 22.68 $\mu g\ h^{-1}\ mg_{cat}^{-1}$ at −1.0 V vs a reversible hydrogen electrode (RHE) in a 0.1 M Na_2SO_4 electrolyte. The Ni/Zn-NPC material can be called a microwave regenerable catalyst because microwave treatment has proven to be a crucial part of the multi-field coupling to detoxify and make the catalyst reactive, further improving its stability. Density functional theory (DFT) was chosen to explore the mechanism of Ni/Zn-NPC for NRR, providing a profound prediction of the structure of the active site and related reaction pathways and revealing that trace Ni doping optimizes the local coordination environment and N_2 adsorption of Zn atoms.

KEYWORDS: electrocatalytic nitrogen reduction, electrocatalyst, microwave regeneration, transient photo-induced voltage, porous carbon catalyst

1. INTRODUCTION

Electrochemical catalytic N_2 reduction reaction (NRR) to NH_3, powered by electric energy from renewable sources, is considered as one of the most promising approaches for N_2 fixation.[1−4] Compared with the traditional Haber−Bosch process, the nitrogen source in NRR is the N_2 molecules in the air, and the protons are supplied by electrical water splitting. Meanwhile, by applying a suitable voltage, electrons are continuously driven toward the electrocatalyst reaction sites for NRR; thus, this procedure requires lower energy.[5−7] The grand challenge in NRR is the design of new electrocatalysts that can ultimately achieve efficient and commercial NH_3 synthesis with high Faraday efficiency and yield rate. Metal−organic framework (MOF)-derived nitrogen-coordinated porous carbon (NPC) has emerged as a potential candidate catalyst for NRR. Since nitrogen element has a higher electronegativity than carbon element, the electron density of carbon is considered to possess more positive charges, which is beneficial to the adsorption of N_2.[8−10] Many nitrogen-doped carbon materials are mainly derived from zeolitic imidazolate framework-8 (ZIF-8)-based MOFs, which are porous materials with adjustable high porosity, a large specific surface area, and an excellent gas adsorption capacity.[11−14] However, a new two-dimensional leaf-like ZIF

(ZIF-L), a polymorphism of ZIF-8, with higher porosity and specific surface area than ZIF-8, has not received significant attention for electrocatalytic NRR application as yet. Notably, ZIF-L exhibits a higher gas adsorption capacity than ZIF-8 under ambient conditions, which implies its potential as a precursor for providing catalytic sites.[15]

Although the atomic-scale reaction process research of NRR has revealed the high atom utilization efficiency of one metal active site, such as Mo, Fe, and Ru, there are still challenges involved due to the multiple reaction intermediates of the NRR.[12,16,17] Bimetallic doping with more flexible sites can effectively adjust the electronic environment around the adsorbed N_2 and synergetic interatomic interactions, thereby disseminating the polarity of N≡N with lower interruption energy. Compared with the single active site, heteronuclear bimetallic sites exhibit superior catalytic activity for carbon dioxide and oxygen reduction reactions, such as Zn/Co−N−C,
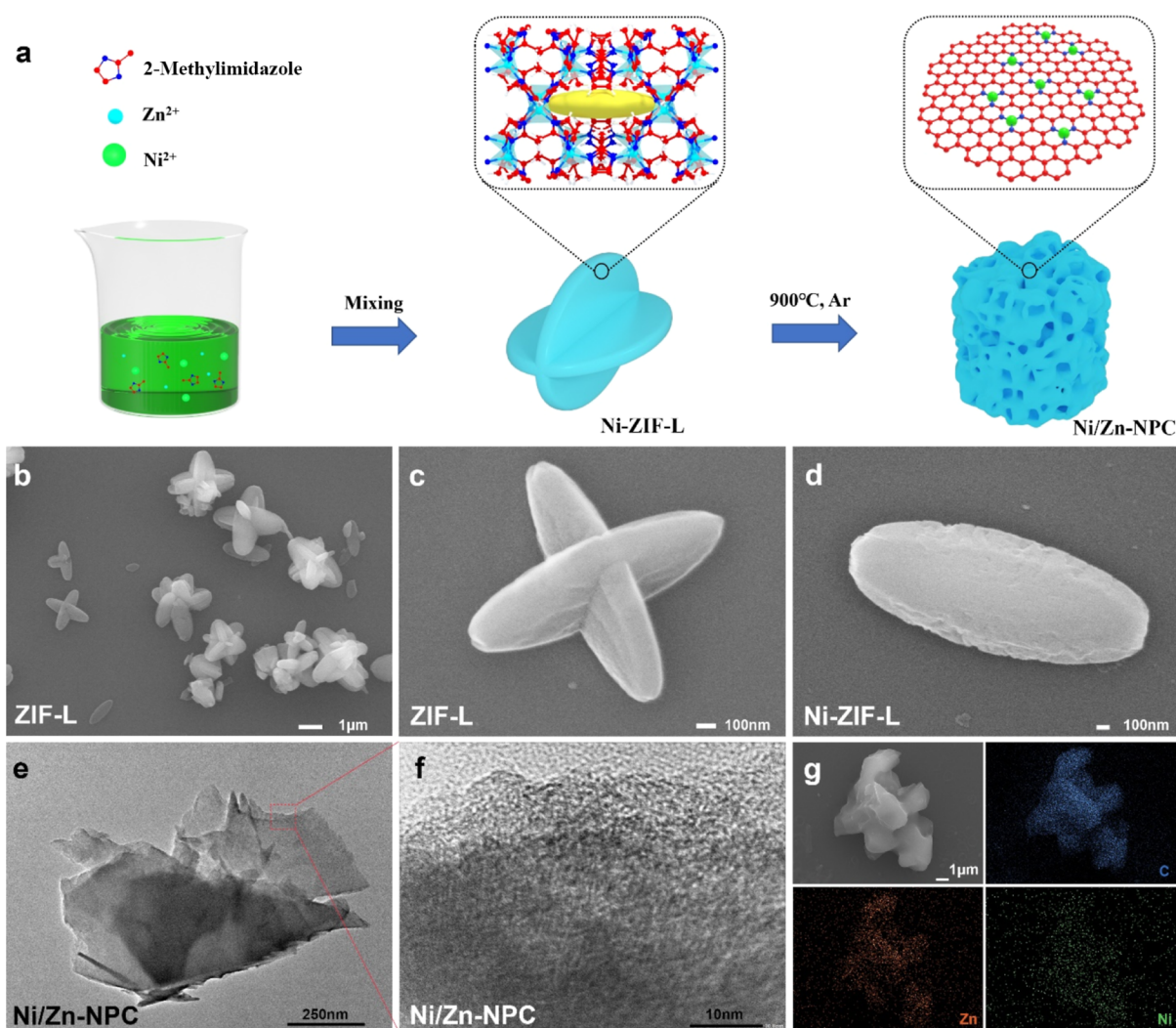
Figure 1. (a) Schematic illustration of Ni/Zn-NPC preparation. The interior image of ZIF-L shows the structure and approximate shape of the cavity (yellow). This structure is obtained from the Cambridge Crystallographic Data Centre (CCDC) (https://www.ccdc.cam.ac.uk/) according to the report from Wang in 2013.[15] The internal structure diagram of Ni/Zn-NPC is a predictive model to show the doping of Ni in nitrogen-coordinated porous carbon; SEM images of (b,c) ZIF-L and (d) Ni-ZIF-L; (e,f) TEM images of Ni/Zn-NPC; and (g) EDS elemental mapping of Ni/Zn-NPC.

Fe/Co−N−C, Ni/Fe−N−C, and Zn/Fe−N−C.[18−21] Considering the different electronegativity of Zn (χ = 1.65) and Ni (χ = 1.91), it can be reasonably speculated that it is easier for Ni to obtain outer electrons from Zn. However, it remains a great challenge to understand their working mechanisms as NRR active sites.

Herein, we report a ZIF-L-derived Ni and Zn bimetallic co-doped nitrogen-coordinated porous carbon (Ni/Zn-NPC) as an electrocatalyst for nitrogen fixation in a neutral electrolyte. The experimental results demonstrated that Ni could promote electron transition from graphitic N to the edge of N active sites that include pyrrolic and pyridinic N. The edge of defective N was proven to have a higher nitrogen adsorption energy than graphitic N, which was more conducive to the NRR.[22] When tested in 0.1 M Na_2SO_4 electrolyte, Ni/Zn-NPC achieved a high NH_3 yield of 22.68 μg h^{-1} mg$_{cat}$$^{-1}$ at −1.0 V (vs RHE). Microwave treatment has proved to be a crucial part of the multi-field coupling to detoxify and regenerate the catalyst and also improve its stability. Furthermore, density functional theory (DFT) calculations were employed to understand the possible structures of active sites and favorable

reaction pathways of the NRR on Ni/Zn-NPC. The introduction of Ni can optimize the electronic structure around the Zn site and thus facilitate the adsorption of N_2 on the Zn atom.

2. RESULTS AND DISCUSSION

Ni/Zn-NPC was prepared from Ni-ZIF-L precursors by the pyrolysis process (Figure 1a). First, Ni-ZIF-L (MOF, consisting of Ni^{2+}, Zn^{2+}, and 2-methylimidazole) was prepared by mixing aqueous zinc nitrate, nickel nitrate, and 2-MeIM. The Ni/Zn atomic ratio was 1:40. Then, Ni-ZIF-L was calcined at 900 °C with a heating rate of 5 °C min^{-1} under N_2 flow for 3 h in a tube furnace to obtain the Ni/Zn-NPC electrocatalyst. In contrast, Zn-NPC without Ni doping was synthesized from ZIF-L by the same pyrolysis method. X-ray diffraction (XRD) was conducted to investigate the structures and composition of the obtained samples. Figure S1 shows the XRD patterns of Ni-ZIF-L, ZIF-L, and the simulated ZIF-L, which prove that the obtained precursors successfully retained the ZIF-L structures.[15] Similar XRD patterns demonstrate that there is no obvious crystal structure distortion due to the
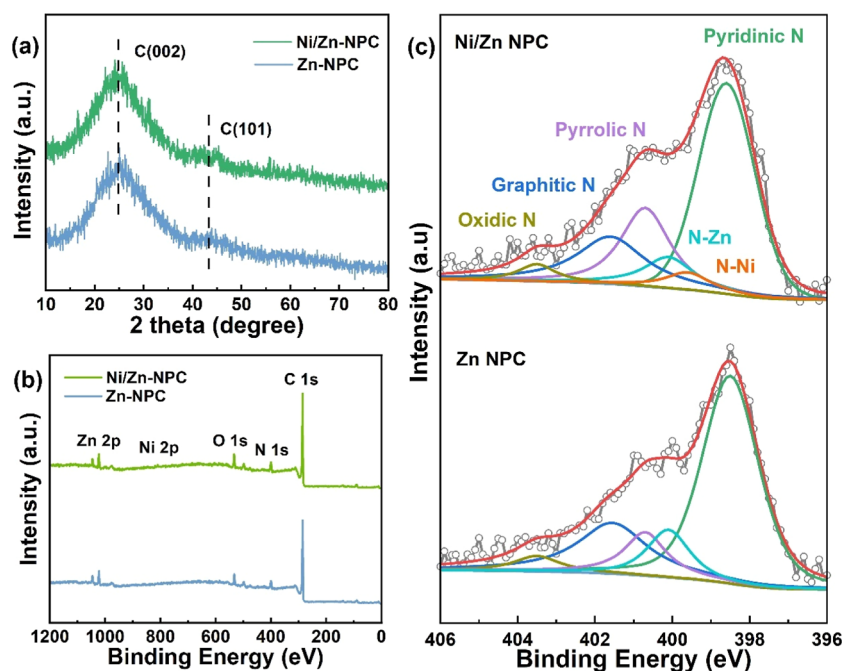
Figure 2. (a) XRD patterns of Ni/Zn-NPC and Zn-NPC; (b) XPS survey spectra of Ni/Zn-NPC and Zn-NPC; and (c) XPS spectra of N1s for Zn-NPC and Ni/Zn-NPC.

doping of Ni. The XRD patterns of Ni/Zn-NPC and Zn-NPC are displayed in Figure 2a. Both Ni/Zn-NPC and Zn-NPC exhibited two broad peaks, (002) and (101) facets of graphitic carbon, which are located at 24.1 and 43.3°, respectively. These results indicated that the regular MOF structure was transformed into amorphous graphite carbon after pyrolysis. Compared with the almost insulated ZIF-L, the conductivity can be enhanced by the conversion to disordered amorphous carbon, which is also beneficial for electrocatalysis applications.[23] Structures based on Ni and Zn (such as NiO, Ni, and ZnO) were not detected.

X-ray photoelectron spectroscopy (XPS) was employed to further explore the structure and element valences. As shown in Figure 2b, the Zn 2p, O 1s, N 1s, and C 1s peaks were detected at 1044.8, 531.8, 398.4, and 285 eV, respectively. A faint peak of Ni 2p appeared at 852.6 eV only in the Ni/Zn-NPC curve, which proved the existence of Ni at the surface of Ni/Zn-NPC. The same electronic orbit peaks also appeared in the XPS survey spectra of ZIF-L and Ni-ZIF-L (Figure S2), which illustrated the inheritance of element types during the pyrolysis. The XPS spectrum of N 1s was considered as the combination of oxidic N, graphitic N, pyrrolic N, and pyridinic N at 403.5, 401.1, 400.2, and 398.6 eV, respectively.[24] Edge nitrogen (pyrrolic N and pyridinic N) has been proven to possess excellent nitrogen adsorption capacity, which provides an enhanced potential for electrocatalytic nitrogen reduction.[22,25] As shown in Figure 2c, compared with the proportion of marginal N in Zn-NPC, the ratio of that in Ni/Zn-NPC was reserved, implying the maintenance of lattice distortion due to introducing Ni and a higher NRR yield rate of Ni/Zn-NPC. N−Ni and N−Zn coordination can be found at 399.6 and 400.1 eV,[26] respectively, which is similar to the positions for Ni and Zn sites.[27] The presence of N species is further confirmed by the C−N peak at 285.9 eV in the C 1s spectrum (Figure S3). A weak peak signal of Ni 2p is located between Ni^{2+} (~857.1 eV) and Ni^{0} (~852.7 eV) (Figure S3), indicating the

presence of Ni(I) species, which matched with the N−Ni peak in N 1s.[28−30]

According to the previously mentioned synthesis method, a typical ZIF-L structure in scanning electron microscopy (SEM) was obtained, as shown in Figure 1b,c. Compared with the SEM image of Ni-ZIF-L (Figure 1d), ZIF-L modified by trace Ni element still maintained a leaf-like morphology, indicating that the modification of Ni may cause lattice distortion instead of macroscopic morphological changes. The obtained ZIF-L and Ni-ZIF-L have an elliptical blade morphology with an average length of 2 μm and a width of 500 nm, while the cross-growing leaves can clearly show their thickness of around 120 nm (Figure S4). The transmission electron microscopy (TEM) morphology of Ni/Zn-NPC after carbonization is shown in Figure 1e,f. The intense high-temperature carbonization reaction destroyed the regular structure of Ni-ZIF-L, accompanied by the collapse of micropores and reconnection of C−C, C−N, and C−Zn bonds. Part of the Ni atoms would be anchored in the regular tetrahedron polygon of N instead of Zn. The edges of the carbonized Ni/Zn-NPC are displayed under HRTEM with disordered lattice fringes, which is consistent with the result of XRD for amorphous carbon. The SEM image and the corresponding energy-dispersive X-ray spectroscopy (EDS) elemental mapping revealed the distribution of N, Zn, and Ni elements throughout the whole Ni/Zn-NPC structure (Figure 1g). According to the EDX sum spectrum quant results (Figure S5), the atomic ratio of metallic elements Ni/Zn is approximately 1:37.

Raman spectra were employed to analyze the defective condition of porous carbon. It can be found that in both Zn-NPC and Ni/Zn-NPC, a slight and gradual peak is observed at 2730 cm^{-1} attributed to the 2D band of graphite, shown in Figure S6,[29] which agreed with the XRD results for graphitic carbon peaks. Furthermore, D and G bands of graphitic carbon can be observed clearly at the peaks of 1320 and 1580 cm^{-1},[29] respectively. The intensity ratio of the D/G band (I_D/I_G) is
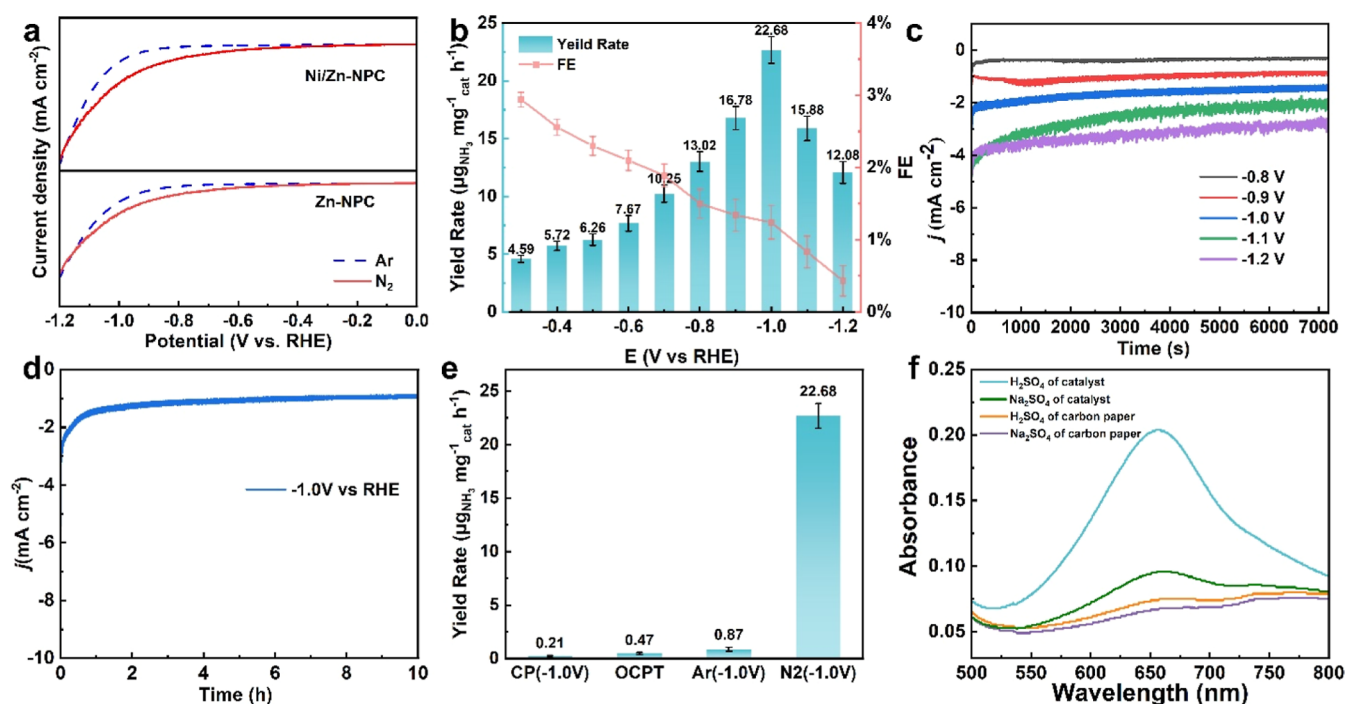
Figure 3. (a) LSV curves of Ni/Zn-NPC and Zn-NPC in Ar and N_2 saturated 0.10 M Na_2SO_4; (b) NH_3 formation rates and FE of Ni/Zn-NPC at different potentials; (c) current density curves of Ni/Zn-NPC from −0.8 V to −1.2 V (vs RHE) during 2 h reaction; (d) time-dependent current density curve of Ni/Zn-NPC for 10 h NRR at −1.0 V vs RHE; (e) UV−vis absorption spectrum of Ni/Zn-NPC catalyst (−1.0 V vs RHE) and CP; and (f) comparison of yields under N_2, Ar (−0.8 V vs RHE), and OCPT.

considered to represent the graphitization level, while the D/G band of Ni/Zn-NPC (I_D/I_G = 1.125) is higher than that of Zn-NPC (I_D/I_G = 1.055), which implies that more defects are developed in Ni/Zn-NPC. The active sites provided by the defects will facilitate electrocatalytic nitrogen reduction.[30] Meanwhile, Ni/Zn co-doping may be another reason for the increase in the disorder of the carbon plane.[31] We also used BET to investigate the specific surface area and pore width distribution of Ni/Zn-NPC and Zn-NPC. Figure S7 shows that type IV curves represented micropores on both NPCs, which could be confirmed by their pore width distribution curves (Figure S8). The Brunauer−Emmett−Teller (BET) specific surface area of Ni/Zn-NPC is 422.99 m^2 g^{-1}, higher than that of Zn-NPC with 366.68 m^2 g^{-1}. The micropore volumes of Ni/Zn-NPC and Zn-NPC were 0.193 and 0.174 cm^3 g^{-1}, respectively. In a porous architecture, a large surface area could accommodate nitrogen adsorption and provide active sites, which is beneficial for promoting three-phase contact between nitrogen, the electrocatalyst, and the aqueous electrolyte. As per the results of the BJH (Barrett−Joyner−Halenda) method, Ni/Zn-NPC and Zn-NPC exhibit dominant micropores concentrated at ∼2.2 and ∼2.3 nm, respectively.

To preliminarily explore the NRR activity of Ni/Zn-NPC and Zn-NPC, LSV curves were obtained in Ar- and N_2-saturated 0.1 M Na_2SO_4 electrolytes. The reaction took place at ambient temperature and used the same H-cell system (Figures S9 and S10). As shown in Figure 3a, the cathodic current curves of both Ni/Zn-NPC and Zn-NPC start to rise from −0.4 V (vs RHE). A more negative current density could be observed on the N_2 curve compared with that of Ar, which could indicate supplementary promotion from NRR. The violent hydrogen evolution reaction (HER) dominant electrode has more negative bias voltages when the voltage is greater than −1.1 V. The polarization current density curves in

N_2 and Ar gradually coincided. According to the range of difference between the current density curves, the rational potential range of NRR is from −0.4 to −1.1 V (vs RHE). As expected, both Ni/Zn-NPC and Zn-NPC were active for electrochemical NRR. Meanwhile, the net current density of Ni/Zn-NPC for NRR (j_{N_2}−j_{Ar}) was higher than that of Zn-NPC at the same potential, which implies that Ni/Zn-NPC is more active than Zn-NPC for the electrochemical reduction of N_2.

The performance of Ni/Zn-NPC for electrocatalytic NRR was further assessed by electrolyzing N_2 at a constant potential. The indophenol blue method was used for the detection of the produced ammonia (shown in the Supporting Information with calibration curves, Figures S11 and S12). Figure 3b demonstrates the NH_3 formation rates and FE of Ni/Zn-NPC at different potentials from −0.3 to −1.2 V (vs RHE). The UV−vis raw data for calculating yield rates are shown in Figure S12c,d. The highest NH_3 yield of 22.68 μg h^{-1} mg$_{cat}$$^{-1}$ was achieved at −1.0 V versus RHE, while the FE at that potential maintained a relatively low level at 1.24%. Compared with various N-doped carbon catalysts listed in Table S1, Ni/Zn-NPC shows higher NH_3 formation rates. Current density curves in the 2 h reaction of Ni/Zn-NPC from −0.8 to −1.2 V (vs RHE) recorded in a N_2-saturated electrolyte showed that the current density remained almost stable at lower potentials. However, at higher potentials, such as −1.1 and −1.2 V, the current density decreased as the reaction was carried out; yet finally, it could still maintain a higher level than the current density at a lower potential (Figure 3c). As shown in Figure S13, the performance of Zn-NPC was also evaluated under N_2 as a comparison with Ni/Zn-NPC at the same potential (−1.0 vs RHE). Zn-NPC exhibited an ammonia production rate of 9.93 μg h^{-1} mg$_{cat}$$^{-1}$, which is lower than that of Ni/Zn-NPC.
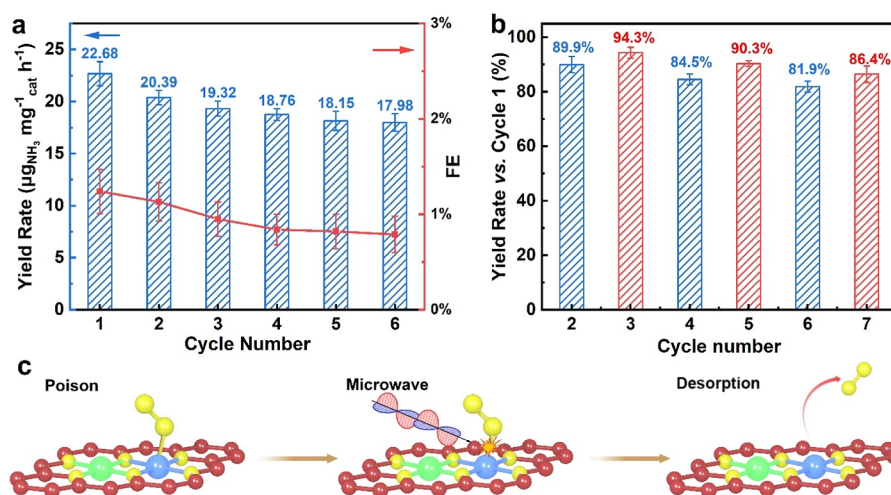
Figure 4. (a) NH_3 formation rates and FE for cyclic stability; (b) percentage stability of NH_3 formation rates compared with that of cycle 1. The red columns represent the yield after microwave activation after cycles 2, 4, and 6; and (c) schematic illustration of the microwave treatment detoxification process.

Ni/Zn-NPC was bathed in a 6 M HCl solution for 30 min to remove Ni and Zn and to obtain NPC without metal doping. NPC was proven to have lesser N, Ni, and Zn content through the XPS survey, as compared with Ni/Zn-NPC (Table S2). The ammonia yield of NPC under the same conditions was 10.64 $\mu g\ h^{-1}\ mg_{cat}^{-1}$, suggesting that Zn-NPC and NPC have no advantage for electrochemical ammonia synthesis, but Ni/Zn-NPC has a synergistic effect for NRR.

In order to test the stability of the Ni/Zn-NPC catalyst for NRR, a working electrode prepared with carbon paper loaded with Ni/Zn-NPC was recycled six times with a 2 h reaction time for every cycle. As shown in Figure 4, the NH_3 formation rate gradually declines after the second cycle and finally stabilizes at around 13 $\mu g\ h^{-1}\ mg_{cat}^{-1}$, which is still higher than the yield of NPC. In contrast, FE does not decrease significantly and fluctuates at around 1.00%. The decline in activation might initially be due to poisoning by NH_3 and H_2O, which could not be ignored for transition-metal nitride catalysts during the process of NRR.[32] To ascertain that the catalysts are indeed poisoned, the catalyst-supported carbon paper before and after the electrochemical reaction was examined by Fourier transform infrared spectroscopy (FTIR). The resulting spectra showed slightly different characteristics at 1110−1150 cm^{-1}, corresponding to N−N stretching[29,33] (Figure S14a). Thus, it is possible for an intermediate containing N−N to gradually occupy the reaction site during the reduction process. Pulsed microwave treatment is considered to continuously provide strong energy to desorb toxic molecules from the active sites and reactivate the catalyst surface (Figure 4c).[34] Thus, the recycled carbon paper electrode was treated in a 250 W high-power microwave for 30 s before the next reaction cycle. Figure 4b shows the cycle stability yield after alternating microwave reactivation after cycles 2, 4, and 6, which was the percentage stability compared with the yield of cycle 1. The reactivated yields represented by the red column are significantly higher than that of the corresponding cycle number in Figure 4a, which indicates that the multi-field coupling mechanism of the microwave activation treatment can alleviate the poisoning of the catalyst surface and further reactivate the catalyst. We investigate the catalyst after microwave treatment, and the resulting FTIR curve is shown in Figure S14a and integrated with curves

obtained after and before the nitrogen reduction reaction. After microwave treatment, the peak decreases obviously, but there is still a slight difference and it does not return to the same level as that before the reaction, which is consistent with the stability test where performance was always enhanced after microwave treatment but could not reach the 100% performance of the first cycle. The stability of the Ni/Zn-NPC catalyst is investigated by a 10 h electrocatalytic test. As shown in Figure 3d, a stable current density curve of Ni/Zn-NPC for 10 h at −1.0 V is achieved.

Nitrogen was detected through XPS, which indicates that Ni/Zn-NPC may provide some nitrogen source that could be subsequently converted into ammonia. To eliminate the effect of the nitrogen element in the catalyst, argon instead of nitrogen was filled in the reaction chamber to detect the yield of ammonia (Figure 3e). We compared the ammonia yield at −1.0 V versus RHE, which was 0.87 $\mu g\ h^{-1}\ mg_{cat}^{-1}$ in argon. A slight ammonia yield in argon might exclude the effect of the nitrogen contained in the catalyst itself. The source of nitrogen can also be corroborated by ^{15}N isotope testing.[35] From Figure S14b, the characteristic peaks of $^{14}NH_4^+$ and $^{15}NH_4^+$ could be detected when using the corresponding feeding gas, indicating that the produced ammonia originates from the fed nitrogen.[36] Similarly, we carried the catalytic system under open-circuit potential−time (OCPT) mode to exclude the possibility that the catalyst could release gas under N_2. The ammonia yield under this condition was 0.47 $\mu g\ h^{-1}\ mg_{cat}^{-1}$, which is much lower than that in nitrogen and argon, indicating that the catalyst has no nitrogen reduction performance at the empty potential. The effect of carbon paper (CP) was also considered through comparative experiments. Figure 3f exhibits the UV−vis absorption spectra of the Ni/Zn-NPC catalyst (−1.0 V vs RHE) and only CP. The acid trap (0.05 M H_2SO_4) and electrolyte (0.1 M Na_2SO_4) were tested separately. There is an obvious peak of the acid trap after electrocatalytic reduction of nitrogen with the catalyst, compared with the acid trap absorbance of CP, which illustrates the obvious performance of the catalyst in fixing nitrogen and excludes the influence of CP. Hydrazine is one of the products of electrocatalytic reduction of nitrogen, the content of which represents the selectivity of the catalyst. The absorption curve of hydrazine produced by Ni/Zn-NPC at −1.0 V (vs RHE) is close to the 0 mg L^{-1}
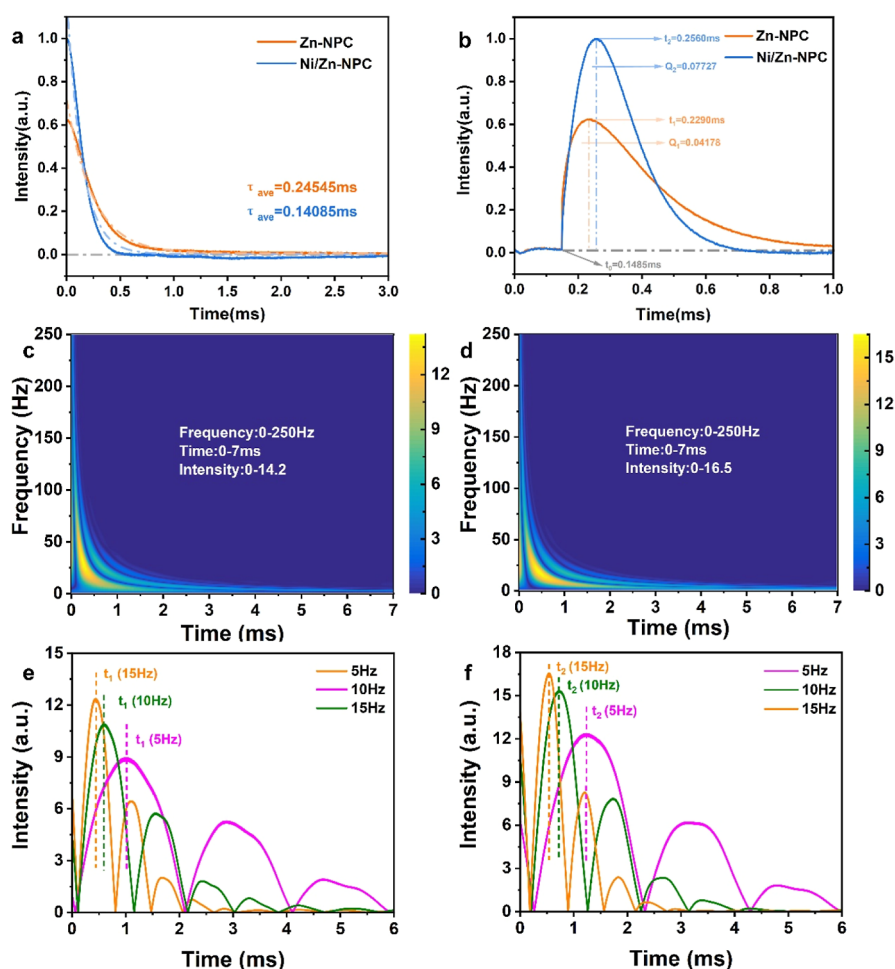
Figure 5. (a) TPV decay curve and the average electron relaxation time of Zn-NPC and Ni/Zn-NPC; (b) TPV curve of Zn-NPC and Ni/Zn-NPC and their Q and Δt; CWT patterns of (c) Ni/Zn-NPC and (d) Zn-NPC; and intensity−time curve of (e) Ni/Zn-NPC and (f) Zn-NPC at 5, 10, and 15 Hz.

standard curve, which means that there is almost no hydrazine produced by Ni/Zn-NPC (Figures S15 and S16). This catalyst has excellent selectivity for electrochemical ammonia synthesis.

The electrochemical characteristics of the catalyst were analyzed to explore the influencing factors on the catalytic performance. Cyclic voltammetry could be used to measure the electrochemical active surface area (ECSA) (Figure S17).[37,38] According to the CV curves, the fitting lines of electric layer capacities could be calculated in Figure S18. With the same area of 1 cm^2 of the CP working electrode, the ECSAs of Ni/Zn-NPC and Zn-NPC were 0.219 and 0.0594 mF, respectively. Because N-coordinated porous carbon is not a conductor or semiconductor, their ECSA maintained a low level. Ni/Zn-NPC shows a higher ESCA than that of Zn-NPC, which implies the promotion effect of doping Ni. In addition, electrochemical impedance spectroscopy (EIS) was used to evaluate the resistance of electron transfer for the electro-catalyst.[23] In Figure S19a, at the high-frequency region, Ni/Zn-NPC exhibits a smaller arc radius. Then, at the low-frequency region (Figure S19b), Ni/Zn-NPC has a steeper line, indicating better conductivity and a smaller impedance obviously. Thus, Ni doping is an effective strategy to enhance electron transfer.

Based on the previous stimuli-response method, the transient photo-induced voltage (TPV) measurement was carried out for the electron-transfer behavior in the electro-

catalyst interface.[39,40] The typical TPV decay curves of Ni/Zn-NPC and Zn-NPC are shown in Figure 5a. Both decay sharply at the initial stage, indicating favorable electrical conductivity. From the aspect of dynamics, the average electron relaxation time (τ_{ave}) was obtained according to the TPV decay curve fitting calculation. The lower decay rate of Ni/Zn-NPC (τ_{ave} = 0.14085 ms) possesses better electron-transfer performance than that of Zn-NPC (τ_{ave} = 0.24545 ms). We also calculated the relative charge-transfer rate 'v' of different catalysts according to $v = Q/\Delta t$, where Q is the total amount of charge generated during this process from the time when hot electrons are excited on the surface of the catalyst until the charge begins to decay, and Δt is the time for the charge to decay from the beginning to the complete decay. According to Q and Δt values (Figure 5b), the relative charge-transfer rate of Ni/Zn-NPC is 0.7188, which is higher than that of Zn-NPC, which is 0.519. To further evaluate the interface charge transfer, the TPV decay curves were converted to signal amplitude as a function of frequency (Hz) by the fast Fourier transform (FFT). The peak amplitude corresponds to the signal frequency components at different frequencies. Mean-while, considering the relationship between time and these frequency components, using the continuous wavelet trans-form (CWT) process, the TPV decay curves were converted to a TPV dynamic relaxation curve signal with relevance between frequency, time, and amplitude. According to the FFT results
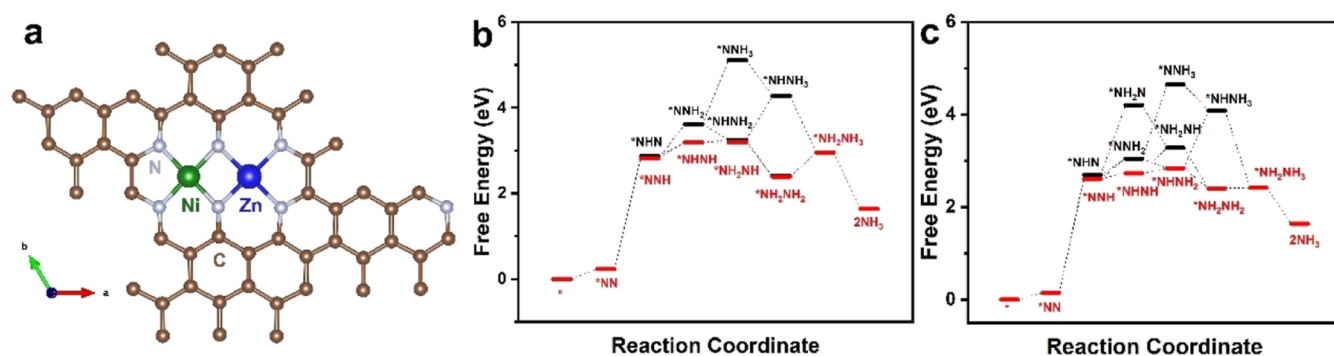
Figure 6. (a) Schematic diagram of Ni−Zn−N$_6$ diatomic structure; free-energy diagram of the N$_2$ electrochemical reduction on (b) Ni and (c) Zn atom site of Ni−Zn−N$_6$. The red line represents the most likely reaction path with the lowest energy.
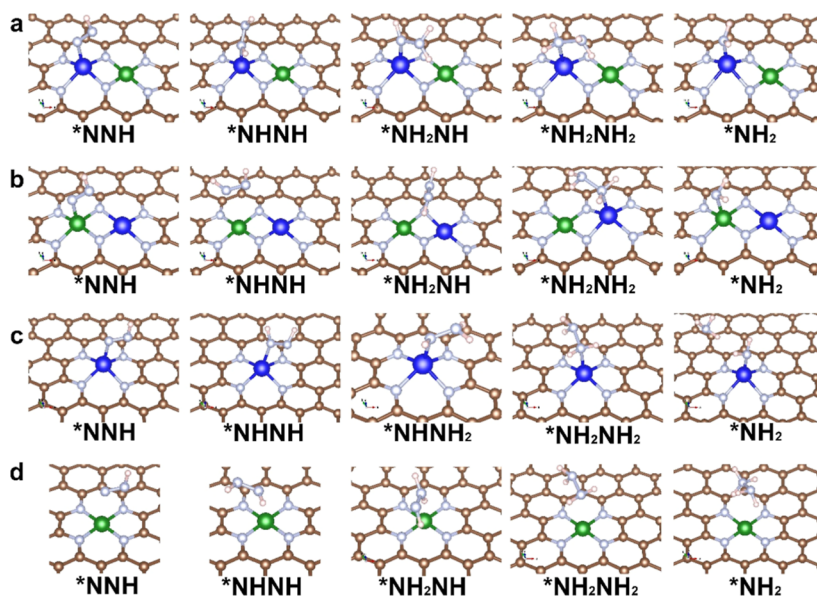

Figure 7. Structure models of intermediates with an alternating pathway for (a) Zn of Ni−Zn−N$_6$, (b) Ni of Ni−Zn−N$_6$, (c) Zn−N$_4$, and (d) Ni−N$_4$. The blue, green, cyan, brown, and pink spheres represent Zn, Ni, N, C, and H atoms, respectively.

of Ni/Zn-NPC and Zn-NPC (Figure 5c,d), the doping of Ni broadens the range of interfacial charge transfer with higher amplitude in the high-frequency region (300−400 Hz), which is more clearly shown in the 3d CWT spectra (Figure S20). Thus, Ni could accelerate the charge transfer while maintaining a good, narrow electron-transfer speed distribution and charge-transfer intensity, which is conducive to electrochemical reactions.

The dynamics of the electron transport process could be understood by the relationship between intensity and time of peak positions at different frequencies (1, 3, 5, 10, and 15 Hz).[41] As shown in Figures 5e and S20c, the peak positions of Ni/Zn-NPC (t_1 X Hz, X represents different frequencies) are 1.614 ms (t_1 1 Hz), 1.456 ms (t_1 3 Hz), 1.018 ms (t_1 5 Hz), 0.594 ms (t_1 10 Hz), and 0.447 ms (t_1 15 Hz). Correspondingly, the peak positions of Zn-NPC (t_2 X Hz) are 5.348, 1.904, 1.237, 0.726, and 0.543 ms, shown in Figures 5f and S20d. The time difference (Δt: $t_2X − t_1X$) at the same frequency could show the charge-transfer velocity of Ni/Zn-NPC and Zn-NPC, which is shown in Figure S20e. The initial Δt is large at 3.734 at 1 Hz, and with increasing frequencies, Δt gradually reduces to near zero, while the charge-transfer velocity of Ni/Zn-NPC is obviously enhanced in the lower frequency scale region. Ni effectively improves the transfer rate

of slow electrons at the interface of Zn-NPC, thus accelerating the electron supply rate in the electrocatalytic process.[42] The transfer rate of fast electrons is also enhanced slightly.

The theoretical insight of higher catalytic performance for Ni/Zn-NPC was further investigated by DFT calculation.[43,44] In order to explore the underlying surface reaction mechanism, we intend to use a two-dimensional graphite surface to explore the effects of Ni doping on the surface microstructure. Structures of nitrogen-coordinated porous carbons derived from MOFs, especially ZIF-8 possessing a similar topology as ZIF-L, have been widely researched, including Fe−Cu,[45,46] Fe−Zn,[47] Zn−Co,[48] Fe−Mo,[49] Cu−Sn,[50] Ni−Fe,[51,52] Ni−Cu,[53] and Fe−Pt.[54] 4-N coordination and 3-N coordination mainly account for most of the cases in similar models. Compared with the 4-N-coordinated model in Figure 6a, metal elements in the 3-N-coordinated model escape from the 2D carbon surface when we perform the preliminary relaxation process. Thus, the 4-N coordination model was further discussed as a more potential surface reaction site. We calculated the Gibbs free energy (G) for each step involved in the N$_2$ reduction at 0 V versus RHE on the possible diatomic model (Ni−Zn−N$_6$) as shown in Figure 6a. For comparison, the intermediate products and free energy of single-atom structure models Ni−N$_4$ and Zn−N$_4$ were also

considered in Figure S21. For the diatomic model, N_2 molecules can initially be adsorbed separately on Ni or Zn atoms until the completion of hydrogenation. Figure S22 shows a stable absorption structure on the Zn and Ni atoms after one atom hydrogenation at the proximal end. As shown in Figures 6b,c and S23, the associative alternating pathway is the optimal response pathway for all absorption models. The only subtle path difference is that N_2 will preferentially select the near-end N atom for third hydrogenation when it is adsorbed on the Zn atom both in the single-atom model and the diatomic model. The stable reaction intermediate state models are shown in Figure 7. After comparing the key reaction parameters in Table S3, the higher NRR performance of Ni/Zn-NPC was further revealed. Doping Ni effectively reduces the N_2 adsorption energy on the Zn atom from 0.228 eV in Zn−N_4 to 0.148 eV in Ni−Zn−N_6, while the hydrogen evolution performance is simultaneously suppressed from 1.25 to 1.65 eV, shown in Figure S24. According to the DFT calculations, the formation of diatomic sites by Ni doping promotes the NRR at Zn sites, while Ni sites are still maintained inactively. As a control experiment, under the premise that total metal cations are consistent with Ni-ZIF-L, we adjusted the atomic ratio of Ni/Zn to 1:9 and 1:3 to obtain Ni_1/Zn_9-NPC and Ni_1/Zn_3-NPC, respectively, with the same crystal structure as Ni/Zn-NPC according to their XRD results (Figure S25). The highest ammonia yield of these samples is lower than that of Ni/Zn-NPC (shown in Figure S26).

3. CONCLUSIONS

In summary, we developed a ZIF-L-derived Ni/Zn-NPC catalyst for cost-effective ammonia synthesis from the electrochemical reduction of N_2. Ni/Zn-NPC achieved a high ammonia production rate of 22.68 μg h^{-1} mg_{cat}^{-1} at −1.0 V versus RHE, while the FE at that potential was maintained at 1.24%. Zn-NPC and NPC without metal doping exhibited lower yields, which indicated that the activity sites of Ni and Zn co-doped catalysts had a synergistic effect on enhancing the NRR. The electrochemical test also illustrated the better NRR performance of Ni/Zn-NPC. According to the DFT calculation, the formation of diatomic sites by Ni doping promotes the NRR at Zn sites with a lower nitrogen adsorption energy and a higher energy barrier for the HER. This work provides an optimized solution for low-cost atomic-level nitrogen-doped carbon catalysis and paves a new avenue for further research of carbon-based atomic catalysts.

4. EXPERIMENTAL SECTION

4.1. Synthesis of ZIF-L, Zn-NPC, and Ni/Zn-NPC. *4.1.1. Preparation of ZIF-L.* In a typical experiment, $Zn(NO_3)_2\cdot6H_2O$ (1.041 g) was dissolved in 7 mL of DI water. 2-MeIM (4.598 g) was dissolved in 70 mL of DI water. The above 2-MeIM solution was added to the $Zn(NO_3)_2\cdot6H_2O$ solution drop by drop in an injection syringe with a 5 mL min^{-1} injection rate. The mixed solution was kept under vigorous stirring at 25 °C for 1 h. The as-obtained precipitate was separated by centrifugation and washed with DI water and methanol 3 times. Finally, the dried ZIF-L sample was obtained after being kept overnight at 60 °C under vacuum.

4.1.2. Synthesis of Zn-NPC. The obtained ZIF-L was heated at 900 °C with a heating rate of 5 °C min^{-1} under N_2 flow for 3 h in a tube furnace. After the temperature of the tube furnace naturally dropped to room temperature, Zn-NPC was obtained and it could be used as a catalyst directly.

4.1.3. Synthesis of Ni/Zn-NPC. $Zn(NO_3)_2\cdot6H_2O$ (4.598 g) and $Ni(NO_3)_2\cdot6H_2O$ (0.0254 g) were dissolved in 7 mL of DI water. The

molar ratio of Ni^{2+} and Zn^{2+} was kept at 1:40. Then, the obtained solution was dropwise added to 70 mL of DI water containing 4.597 g of 2-MeIM. After vigorous stirring at 25 °C for 1 h, the as-obtained precipitate (denoted as Ni-containing derivative of ZIF-L) was separated by centrifugation and washed with DI water and methanol 3 times, separately. Then, the Ni-containing derivative of ZIF-L was dried at 60 °C under vacuum overnight. Finally, the dried derivative was heated at 900 °C at a heating rate of 5 °C min^{-1} under N_2 flow for 3 h in a tube furnace, in which the process was similar to that for Zn-NPC. The Ni and Zn nanoparticles decorated on nitrogen-doped carbon (denoted as Ni/Zn-NPC) were obtained as the catalyst without further treatment after the tube furnace was naturally cooled to room temperature.

4.2. Structural Characterization. SEM images were obtained on a JSM-7800F microscope. The XRD patterns were obtained from a LabX XRD-6100 X-ray diffractometer with Cu Kα radiation (40 kV, 30 mA) of wavelength 0.154 nm (SHIMADZU, Japan). Nitrogen adsorption/desorption isotherms were recorded on an ASAP 2460 instrument. The absorbance data of the spectrophotometer were measured on a SHIMADZU UV-2700 ultraviolet−visible (UV−vis) spectrophotometer. TEM images were obtained on a HITACHI H-8100 electron microscopy (Hitachi, Tokyo, Japan) operated at 200 kV. XPS data of the samples were collected on an ESCALABMK II X-ray photoelectron spectrometer using Mg as the exciting source. Isotope experiments were performed on a 400 MHz nuclear magnetic resonance (NMR) spectrometer (BRUKERAC-P400, Germany).

4.3. Electrochemical Setup. A CHI 660E electrochemical workstation (CHI Instruments, Inc.) was used to collect data and provide catalytic voltage. We used a three-electrode system in the electrochemical measurement in which Ag/AgCl (saturated KCl electrolyte) was used as a reference electrode (RE), the prepared CP loading catalyst (details shown in Supporting Information) was used as the working electrode (WE), and a graphite rod was used as a counter electrode (CE). An H-cell system was used as a reactor with anode and cathode chambers. The H-cell was separated by a Nafion 117 membrane. The potentials were controlled by an electrochemical station. Due to the usage of Ag/AgCl RE, all potentials that we measured were related to Ag/AgCl. The results shown by the standard hydrogen electrode (RHE) were converted from Ag/AgCl by the Nernst equation

$$E\ (\text{vs RHE}) = E\ (\text{vs Ag/AgCl}) + 0.21\ \text{V} + 0.0591 \times \text{pH} \quad (1)$$

4.4. Determination of the NH_3 Yield Rate and Faradaic Efficiency. The production rate of NH_3 was calculated by

$$v[NH_3] = \frac{C_{NH_3} \times V}{t \times m_{cat.}} \quad (2)$$

Here, C_{NH_3} is the measured concentration of NH_4^+ ions, V is the volume of the electrolyte or acid trap, t is the reduction reaction time, and $m_{cat.}$ is the catalyst mass.

Faradaic efficiency can be calculated using the equation

$$\text{FE (\%)} = \frac{3F \times c_{NH_3} \times V}{17 \times Q} \quad (3)$$

where F is the Faraday constant, and Q is the amount of charge which could be obtained by the integral of the $i−t$ curve from the electrochemical workstation.

4.5. DFT Calculations. The DFT calculations in this work were done on the Vienna ab initio simulation package.[55] The K-points were sampled by the Monkhorst−Pack sampling scheme,[56] and the number of K-points along each vector in reciprocal space was set by VASPKIT[57] so that the distance between two neighboring K-points was less than 0.03 Å^{-1}. The energy cutoff was 400 eV, and the inter-atom force was relaxed to less than 0.05 eV/Å. The GGA-PBE (Perdew−Burke−Ernzerhof method of generalized gradient approximation) method[58] was adopted as the exchange−correlation functional, and the projector augmented-wave method[59,60] was selected as the pseudopotential.

ASSOCIATED CONTENT

ⓢ Supporting Information

The Supporting Information is available free of charge at https://pubs.acs.org/doi/10.1021/acsami.3c06037.

Additional experimental details; XRD patterns; XPS spectra and Raman spectra; SEM images; EDX spectrum; N_2 adsorption−desorption isotherms and pore width distribution curves photo of NRR electrochemical tests; schematic diagram of reaction reactor; results of electrochemical tests; UV−vis absorption curves and calibration curves of NRR tests; FTIR spectra of CP loaded Ni/Zn-NPC; ^{1}H NMR spectra of qualitative ^{14}N and ^{15}N isotope tests; 3d CWT spectra; comparison of NRR performance; and DFT calculation (PDF)

AUTHOR INFORMATION

Corresponding Authors

Naiyun Liu − School of Chemistry and Chemical Engineering, Institute for Energy Research of Jiangsu University, Zhenjiang 212013 Jiangsu, China; Email: liuny@ujs.edu.cn

Zhenhui Kang − Institute of Functional Nano & Soft Materials (FUNSOM), Jiangsu Key Laboratory for Carbon-Based Functional Materials & Devices, Soochow University, Suzhou 215123 Jiangsu, China; Macao Institute of Materials Science and Engineering (MIMSE), MUST-SUDA Joint Research Center for Advanced Functional Materials, Macau University of Science and Technology, Taipa 999078 Macao, China; ⓞ orcid.org/0000-0001-6989-5840; Email: zhkang@suda.edu.cn

Haitao Li − School of Chemistry and Chemical Engineering, Institute for Energy Research of Jiangsu University, Zhenjiang 212013 Jiangsu, China; Guangxi Key Laboratory of Electrochemical Energy Materials, Guangxi University, Nanning 530004, China; ⓞ orcid.org/0000-0002-1265-5835; Email: liht@ujs.edu.cn

Authors

Peiji Deng − School of Chemistry and Chemical Engineering, Institute for Energy Research of Jiangsu University, Zhenjiang 212013 Jiangsu, China; Guangxi Key Laboratory of Electrochemical Energy Materials, Guangxi University, Nanning 530004, China; School of Chemical Engineering, University of New South Wales, Sydney 2052 New South Wales, Australia; School of Civil Engineering, The University of Sydney, Sydney 2006 New South Wales, Australia

Yixian Liu − School of Chemistry and Chemical Engineering, Institute for Energy Research of Jiangsu University, Zhenjiang 212013 Jiangsu, China

Yunliang Liu − School of Chemistry and Chemical Engineering, Institute for Energy Research of Jiangsu University, Zhenjiang 212013 Jiangsu, China

Yaxi Li − School of Chemistry and Chemical Engineering, Institute for Energy Research of Jiangsu University, Zhenjiang 212013 Jiangsu, China

Ruqiang Wu − School of Chemistry and Chemical Engineering, Institute for Energy Research of Jiangsu University, Zhenjiang 212013 Jiangsu, China

Lijun Meng − State Key Laboratory of Pollution Control and Resource Reuse, Shanghai Institute of Pollution Control and Ecological Security, School of Environmental Science and Engineering, Tongji University, Shanghai 200092, China

Kang Liang − School of Chemical Engineering, University of New South Wales, Sydney 2052 New South Wales, Australia; ⓞ orcid.org/0000-0003-3985-7688

Yixiang Gan − School of Civil Engineering, The University of Sydney, Sydney 2006 New South Wales, Australia; ⓞ orcid.org/0000-0002-9621-0277

Fen Qiao − School of Chemistry and Chemical Engineering, Institute for Energy Research of Jiangsu University, Zhenjiang 212013 Jiangsu, China

Complete contact information is available at: https://pubs.acs.org/10.1021/acsami.3c06037

Author Contributions

∇P.D. and Y.L. contributed equally.

Notes

The authors declare no competing financial interest.

ACKNOWLEDGMENTS

REFERENCES

(1) Bao, D.; Zhang, Q.; Meng, F.-L.; Zhong, H.-X.; Shi, M.-M.; Zhang, Y.; Yan, J.-M.; Jiang, Q.; Zhang, X.-B. Electrochemical Reduction of N_2 under Ambient Conditions for Artificial N_2 Fixation and Renewable Energy Storage Using N_2/NH_3 Cycle. Adv. Mater. 2017, 29, 1604799.

(2) Soloveichik, G. Electrochemical Synthesis of Ammonia as a Potential Alternative to the Haber−Bosch Process. Nat. Catal. 2019, 2, 377−380.

(3) Yin, Y.; Tan, Y.; Wei, Q.; Zhang, S.; Wu, S.; Huang, Q.; Hu, F.; Mi, Y. Nanovilli Electrode Boosts Hydrogen Evolution: A Surface with Superaerophobicity and Superhydrophilicity. Nano Res. 2021, 14, 961−968.

(4) Wang, R.; He, C.; Chen, W.; Zhao, C.; Huo, J. Rich B Active Centers in Penta-B_2C as High-Performance Photocatalyst for Nitrogen Reduction. Chin. Chem. Lett. 2021, 32, 3821−3824.

(5) Kugler, K.; Ohs, B.; Scholz, M.; Wessling, M. Towards a Carbon Independent and CO_2-Free Electrochemical Membrane Process for NH_3 Synthesis. Phys. Chem. Chem. Phys. 2014, 16, 6129−6138.

(6) Zhuang, Z.; Huang, J.; Li, Y.; Zhou, L.; Mai, L. The Holy Grail in Platinum-Free Electrocatalytic Hydrogen Evolution: Molybdenum-Based Catalysts and Recent Advances. ChemElectroChem 2019, 6, 3570−3589.

(7) Zhuang, Z.; Li, Y.; Huang, J.; Li, Z.; Zhao, K.; Zhao, Y.; Xu, L.; Zhou, L.; Moskaleva, L. V.; Mai, L. Sisyphus Effects in Hydrogen Electrochemistry on Metal Silicides Enabled by Silicene Subunit Edge. Sci. Bull. 2019, 64, 617−624.

(8) Scardamaglia, M.; Amati, M.; Llorente, B.; Mudimela, P.; Colomer, J. F.; Ghijsen, J.; Ewels, C.; Snyders, R.; Gregoratti, L.; Bittencourt, C. Nitrogen Ion Casting on Vertically Aligned Carbon Nanotubes: Tip and Sidewall Chemical Modification. *Carbon* 2014, 77, 319−328.

(9) Chen, X.; Guo, Y.; Du, X.; Zeng, Y.; Chu, J.; Gong, C.; Huang, J.; Fan, C.; Wang, X.; Xiong, J. Atomic Structure Modification for Electrochemical Nitrogen Reduction to Ammonia. *Adv. Energy Mater.* 2020, 10, 1903172.

(10) Yang, Y.; Mao, B.; Gong, G.; Li, D.; Liu, Y.; Cao, W.; Xing, L.; Zeng, J.; Shi, W.; Yuan, S. In-Situ Growth of Zn−AgIn$_5$S$_8$ Quantum Dots on g-C$_3$N$_4$ Towards 0D/2D Heterostructured Photocatalysts with Enhanced Hydrogen Production. *Int. J. Hydrogen Energy* 2019, 44, 15882−15891.

(11) Yang, H.; Lin, Q.; Wu, Y.; Li, G.; Hu, Q.; Chai, X.; Ren, X.; Zhang, Q.; Liu, J.; He, C. Highly Efficient Utilization of Single Atoms Via Constructing 3D and Free-Standing Electrodes for CO$_2$ Reduction with Ultrahigh Current Density. *Nano Energy* 2020, 70, 104454.

(12) Geng, Z.; Liu, Y.; Kong, X.; Li, P.; Li, K.; Liu, Z.; Du, J.; Shu, M.; Si, R.; Zeng, J. Achieving a Record-High Yield Rate of 120.9 for N$_2$ Electrochemical Reduction over Ru Single-Atom Catalysts. *Adv. Mater.* 2018, 30, 1803498.

(13) Zhuang, Z.; Li, Y.; Li, Y.; Huang, J.; Wei, B.; Sun, R.; Ren, Y.; Ding, J.; Zhu, J.; Lang, Z.; Moskaleva, L. V.; He, C.; Wang, Y.; Wang, Z.; Wang, D.; Li, Y. Atomically Dispersed Nonmagnetic Electron Traps Improve Oxygen Reduction Activity of Perovskite Oxides. *Energy Environ. Sci.* 2021, 14, 1016−1028.

(14) Liu, Z.; Du, Y.; Zhang, P.; Zhuang, Z.; Wang, D. Bringing Catalytic Order out of Chaos with Nitrogen-Doped Ordered Mesoporous Carbon. *Matter* 2021, 4, 3161−3194.

(15) Chen, R.; Yao, J.; Gu, Q.; Smeets, S.; Baerlocher, C.; Gu, H.; Zhu, D.; Morris, W.; Yaghi, O. M.; Wang, H. A Two-Dimensional Zeolitic Imidazolate Framework with a Cushion-Shaped Cavity for CO$_2$ Adsorption. *Chem. Commun.* 2013, 49, 9500−9502.

(16) Zhang, R.; Jiao, L.; Yang, W.; Wan, G.; Jiang, H.-L. Single-Atom Catalysts Templated by Metal−Organic Frameworks for Electrochemical Nitrogen Reduction. *J. Mater. Chem. A* 2019, 7, 26371−26377.

(17) Wang, M.; Liu, S.; Qian, T.; Liu, J.; Zhou, J.; Ji, H.; Xiong, J.; Zhong, J.; Yan, C. Over 56.55% Faradaic Efficiency of Ambient Ammonia Synthesis Enabled by Positively Shifting the Reaction Potential. *Nat. Commun.* 2019, 10, 341.

(18) Wang, J.; Huang, Z.; Liu, W.; Chang, C.; Tang, H.; Li, Z.; Chen, W.; Jia, C.; Yao, T.; Wei, S.; Wu, Y.; Li, Y. Design of N-Coordinated Dual-Metal Sites: A Stable and Active Pt-Free Catalyst for Acidic Oxygen Reduction Reaction. *J. Am. Chem. Soc.* 2017, 139, 17281−17284.

(19) Lu, Z.; Wang, B.; Hu, Y.; Liu, W.; Zhao, Y.; Yang, R.; Li, Z.; Luo, J.; Chi, B.; Jiang, Z.; Li, M.; Mu, S.; Liao, S.; Zhang, J.; Sun, X. An Isolated Zinc−Cobalt Atomic Pair for Highly Active and Durable Oxygen Reduction. *Angew. Chem., Int. Ed.* 2019, 58, 2622−2626.

(20) Zhang, L.; Fan, G.; Xu, W.; Yu, M.; Wang, L.; Yan, Z.; Cheng, F. Isolated Diatomic Zn−Fe in N-Doped Carbon for Electrocatalytic Nitrogen Reduction to Ammonia. *Chem. Commun.* 2020, 56, 11957−11960.

(21) Zeng, Z.; Gan, L. Y.; Bin Yang, H.; Su, X.; Gao, J.; Liu, W.; Matsumoto, H.; Gong, J.; Zhang, J.; Cai, W.; Zhang, Z.; Yan, Y.; Liu, B.; Chen, P. Orbital Coupling of Hetero-Diatomic Nickel-Iron Site for Bifunctional Electrocatalysis of CO$_2$ Reduction and Oxygen Evolution. *Nat. Commun.* 2021, 12, 4088.

(22) Mukherjee, S.; Cullen, D. A.; Karakalos, S.; Liu, K.; Zhang, H.; Zhao, S.; Xu, H.; More, K. L.; Wang, G.; Wu, G. Metal-Organic Framework-Derived Nitrogen-Doped Highly Disordered Carbon for Electrochemical Ammonia Synthesis Using N$_2$ and H$_2$O in Alkaline Electrolytes. *Nano Energy* 2018, 48, 217−226.

(23) Luo, S.; Li, X.; Wang, M.; Zhang, X.; Gao, W.; Su, S.; Liu, G.; Luo, M. Long-Term Electrocatalytic N$_2$ Fixation by MOF-Derived Y-

Stabilized ZrO$_2$: Insight into the Deactivation Mechanism. *J. Mater. Chem. A* 2020, 8, 5647−5654.

(24) Zheng, Y.; Jiao, Y.; Li, L. H.; Xing, T.; Chen, Y.; Jaroniec, M.; Qiao, S. Z. Toward Design of Synergistically Active Carbon-Based Catalysts for Electrocatalytic Hydrogen Evolution. *ACS Nano* 2014, 8, 5290−5296.

(25) Liu, Y.; Su, Y.; Quan, X.; Fan, X.; Chen, S.; Yu, H.; Zhao, H.; Zhang, Y.; Zhao, J. Facile Ammonia Synthesis from Electrocatalytic N$_2$ Reduction under Ambient Conditions on N-Doped Porous Carbon. *ACS Catal.* 2018, 8, 1186−1191.

(26) Deng, W.; Min, S.; Wang, F.; Zhang, Z.; Kong, C. Efficient CO$_2$ Electroreduction to CO at Low Overpotentials Using a Surface-Reconstructed and N-Coordinated Zn Electrocatalyst. *Dalton Trans.* 2020, 49, 5434−5439.

(27) Li, Z.; He, D.; Yan, X.; Dai, S.; Younan, S.; Ke, Z.; Pan, X.; Xiao, X.; Wu, H.; Gu, J. Size-Dependent Nickel-Based Electrocatalysts for Selective CO$_2$ Reduction. *Angew. Chem., Int. Ed.* 2020, 59, 18572−18577.

(28) Yang, H. B.; Hung, S.-F.; Liu, S.; Yuan, K.; Miao, S.; Zhang, L.; Huang, X.; Wang, H.-Y.; Cai, W.; Chen, R.; Gao, J.; Yang, X.; Chen, W.; Huang, Y.; Chen, H. M.; Li, C. M.; Zhang, T.; Liu, B. Atomically Dispersed Ni(I) as the Active Site for Electrochemical CO$_2$ Reduction. *Nat. Energy* 2018, 3, 140−147.

(29) Song, P.; Wang, H.; Cao, X.; Liu, N.; Wang, Q.; Wang, R. Ambient Electrochemical N$_2$ Reduction to NH$_3$ on Nitrogen and Phosphorus Co-Doped Porous Carbon with Trace Iron in Alkaline Electrolytes. *ChemElectroChem* 2020, 7, 212−216.

(30) Li, X.; Li, T.; Ma, Y.; Wei, Q.; Qiu, W.; Guo, H.; Shi, X.; Zhang, P.; Asiri, A. M.; Chen, L.; Tang, B.; Sun, X. Boosted Electrocatalytic N$_2$ Reduction to NH$_3$ by Defect-Rich MoS$_2$ Nanoflower. *Adv. Energy Mater.* 2018, 8, 1801357.

(31) Pan, Y.; Zhang, C.; Liu, Z.; Chen, C.; Li, Y. Structural Regulation with Atomic-Level Precision: From Single-Atomic Site to Diatomic and Atomic Interface Catalysis. *Matter* 2020, 2, 78−110.

(32) Abghoui, Y.; Skúlason, E. Onset Potentials for Different Reaction Mechanisms of Nitrogen Activation to Ammonia on Transition Metal Nitride Electro-Catalysts. *Catal. Today* 2017, 286, 69−77.

(33) Song, P.; Wang, H.; Kang, L.; Ran, B.; Song, H.; Wang, R. Electrochemical Nitrogen Reduction to Ammonia at Ambient Conditions on Nitrogen and Phosphorus Co-Doped Porous Carbon. *Chem. Commun.* 2019, 55, 687−690.

(34) Selvam S, M.; Paramasivan, B. Microwave Assisted Carbonization and Activation of Biochar for Energy-Environment Nexus: A Review. *Chemosphere* 2022, 286, 131631.

(35) Su, J.; Zhao, H.; Fu, W.; Tian, W.; Yang, X.; Zhang, H.; ling, F.; Wang, Y. Fine Rhodium Phosphides Nanoparticles Embedded in N, P Dual-Doped Carbon Film: New Efficient Electrocatalysts for Ambient Nitrogen Fixation. *Appl. Catal., B* 2020, 265, 118589.

(36) Jiang, T.; Li, L.; Li, L.; Liu, Y.; Zhang, D.; Zhang, D.; Li, H.; Mao, B.; Shi, W. Ultra-Thin Shelled Cu$_2$-xS/MoS$_2$ Quantum Dots for Enhanced Electrocatalytic Nitrogen Reduction. *Chem. Eng. J.* 2021, 426, 130650.

(37) Cheng, S.; Li, C.; Yu, Z.; Sun, Y.; Li, L.; Yang, J. Defective S/N Co-Doped Carbon Cloth Via a One-Step Process for Effective Electroreduction of Nitrogen to Ammonia. *RSC Adv.* 2020, 10, 9814−9823.

(38) Zheng, X.; Ji, Y.; Tang, J.; Wang, J.; Liu, B.; Steinrück, H.-G.; Lim, K.; Li, Y.; Toney, M. F.; Chan, K.; Cui, Y. Theory-Guided Sn/ Cu Alloying Foreefficient CO$_2$ Electroreduction at Lowoverpotentials. *Nat. Catal.* 2019, 2, 55−61.

(39) Wu, J.; Zhou, Y.; Nie, H.; Wei, K.; Huang, H.; Liao, F.; Liu, Y.; Shao, M.; Kang, Z. Carbon Dots Regulate the Interface Electron Transfer and Catalytic Kinetics of Pt-Based Alloys Catalyst for Highly Efficient Hydrogen Oxidation. *J. Energy Chem.* 2022, 66, 61−67.

(40) Wu, Q.; Cao, J.; Wang, X.; Liu, Y.; Zhao, Y.; Wang, H.; Liu, Y.; Huang, H.; Liao, F.; Shao, M.; Kang, Z. A Metal-Free Photocatalyst for Highly Efficient Hydrogen Peroxide Photoproduction in Real Seawater. *Nat. Commun.* 2021, 12, 483.

(41) Nie, H.; Liu, Y.; Li, Y.; Wei, K.; Wu, Z.; Shi, H.; Huang, H.; Liu, Y.; Shao, M.; Kang, Z. In-Situ Transient Photovoltage Study on Interface Electron Transfer Regulation of Carbon Dots/$NiCo_2O_4$ Photocatalyst for the Enhanced Overall Water Splitting Activity. *Nano Res.* **2022**, *15*, 1786−1795.

(42) Zhou, Y.; Qi, H.; Wu, J.; Huang, H.; Liu, Y.; Kang, Z. Amino Modified Carbon Dots with Electron Sink Effect Increase Interface Charge Transfer Rate of Cu-Based Electrocatalyst to Enhance the CO_2 Conversion Selectivity to C_2H_4. *Adv. Funct. Mater.* **2022**, *32*, 2113335.

(43) Yang, H.; He, C.; Fu, L.; Huo, J.; Zhao, C.; Li, X.; Song, Y. Capture and Separation of CO_2 on BC_3 Nanosheets: A DFT Study. *Chin. Chem. Lett.* **2021**, *32*, 3202−3206.

(44) Fu, L.; Wang, R.; Zhao, C.; Huo, J.; He, C.; Kim, K.-H.; Zhang, W. Construction of Cr-Embedded Graphyne Electrocatalyst for Highly Selective Reduction of CO_2 to CH_4: A DFT Study. *Chem. Eng. J.* **2021**, *414*, 128857.

(45) An, S.; Wang, L.; Li, G.; Zhu, B.; Jin, Q. Well-Defined Fe/Cu Diatomic Catalysts for Boosted Peroxymonosulfate Activation to Degrade Organic Contaminants. *Sep. Purif. Technol.* **2023**, *316*, 123827.

(46) Ding, Y.; Shi, Y.; Xiong, W.; Sun, J. H.; Li, C.; Zhang, Y. Q.; Guo, J. Insights into N-Coordinated Bimetallic Site Synergy During No Selective Catalytic Reduction by CO. *ACS Appl. Mater. Interfaces* **2021**, *13*, 57182−57192.

(47) Li, Z.; Tian, Z.; Cheng, H.; Wang, T.; Zhang, W.; Lu, Y.; Lai, Y.; He, G. Engineering D-Band Center of FeN_4 Moieties for Efficient Oxygen Reduction Reaction Electrocatalysts. *Energy Storage Mater.* **2023**, *59*, 102764.

(48) Song, C.-L.; He, Q.-T.; Zeng, Z.; Chen, J.-Y.; Wen, T.; Huang, Y.-X.; Zhuang, L.-C.; Yi, W.; Cai, Y.-P.; Hong, X.-J. Isolated Diatomic Zn-Co Metal−Nitrogen/Oxygen Sites with Synergistic Effect on Fast Catalytic Kinetics of Sulfur Species in Li-S Battery. *J. Energy Chem.* **2023**, *79*, 505−514.

(49) Gao, S.; Liu, X.; Wang, Z.; Lu, Y.; Sa, R.; Li, Q.; Sun, C.; Chen, X.; Ma, Z. Spin Regulation for Efficient Electrocatalytic N_2 Reduction over Diatomic Fe-Mo Catalyst. *J. Colloid Interface Sci.* **2023**, *630*, 215−223.

(50) Liu, W.; Li, H.; Ou, P.; Mao, J.; Han, L.; Song, J.; Luo, J.; Xin, H. L. Isolated Cu-Sn Diatomic Sites for Enhanced Electroreduction of CO_2 to CO. *Nano Res.* **2023**, *16*, 8729−8736.

(51) Wang, Q.; Jin, B.; Hu, M.; Jia, C.; Li, X.; Sharman, E.; Jiang, J. N-Doped Graphene-Supported Diatomic Ni−Fe Catalyst for Synergistic Oxidation of CO. *J. Phys. Chem. C* **2021**, *125*, 5616−5622.

(52) Zhang, D.; Peng, Y.; Zhang, L.; Guo, Y.; Liu, L.; Wang, H.; Bian, Z. Synergistic Effect of Atomically Dispersed Fe−Ni Pair Sites for Electrocatalytic Reactions to Remove Chlorinated Organic Compounds. *Chemosphere* **2022**, *303*, 134992.

(53) Cheng, H.; Wu, X.; Feng, M.; Li, X.; Lei, G.; Fan, Z.; Pan, D.; Cui, F.; He, G. Atomically Dispersed Ni/Cu Dual Sites for Boosting the CO_2 Reduction Reaction. *ACS Catal.* **2021**, *11*, 12673−12681.

(54) Wang, S.; Hu, Z.; Wei, Q.; Zhang, H.; Tang, W.; Sun, Y.; Duan, H.; Dai, Z.; Liu, Q.; Zheng, X. Diatomic Active Sites Nanozymes: Enhanced Peroxidase-Like Activity for Dopamine and Intracellular H_2O_2 Detection. *Nano Res.* **2022**, *15*, 4266−4273.

(55) Kresse, G.; Furthmüller, J. Efficient Iterative Schemes for Ab Initio Total-Energy Calculations Using a Plane-Wave Basis Set. *Phys. Rev. B* **1996**, *54*, 11169−11186.

(56) Monkhorst, H. J.; Pack, J. D. Special Points for Brillouin-Zone Integrations. *Phys. Rev. B* **1976**, *13*, 5188−5192.

(57) Wang, V.; Xu, N.; Liu, J.-C.; Tang, G.; Geng, W.-T. Vaspkit: A User-Friendly Interface Facilitating High-Throughput Computing and Analysis Using Vasp Code. *Comput. Phys. Commun.* **2021**, *267*, 108033.

(58) Perdew, J. P.; Burke, K.; Ernzerhof, M. Generalized Gradient Approximation Made Simple. *Phys. Rev. Lett.* **1996**, *77*, 3865−3868.

(59) Kresse, G.; Joubert, D. From Ultrasoft Pseudopotentials to the Projector Augmented-Wave Method. *Phys. Rev. B* **1999**, *59*, 1758−1775.

(60) Blöchl, P. E. Projector Augmented-Wave Method. *Phys. Rev. B* **1994**, *50*, 17953−17979.